Mediterranean winter rainfall in phase with African monsoon during past 1.36 million years

Bernd Wagner[1]*†, Hendrik Vogel[2]†, Alexander Francke[1,3], Tobias Friedrich[4], Timme Donders[5], Jack H. Lacey[6], Melanie J. Leng[6,7], Eleonora Regattieri[8,9], Laura Sadori[10], Thomas Wilke[11], Giovanni Zanchetta[8], Christian Albrecht[11], Adele Bertini[12], Nathalie Combourieu-Nebout[13], Aleksandra Cvetkoska[5,11], Biagio Giaccio[14], Andon Grazhdani[15], Torsten Hauffe[11], Jens Holtvoeth[16], Sebastien Joannin[17], Elena Jovanovska[11], Janna Just[1,18], Katerina Kouli[19], Ilias Kousis[20], Andreas Koutsodendris[20], Sebastian Krastel[21], Markus Lagos[22], Niklas Leicher[1], Zlatko Levkov[23], Katja Lindhorst[21], Alessia Masi[10], Martin Melles[1], Anna M. Mercuri[24], Sebastien Nomade[25], Norbert Nowaczyk[26], Konstantinos Panagiotopoulos[1], Odile Peyron[17], Jane M. Reed[27], Leonardo Sagnotti[28], Gaia Sinopoli[10], Björn Stelbrink[11], Roberto Sulpizio[29,30], Axel Timmermann[31,32], Slavica Tofilovska[22], Paola Torri[33], Friederike Wagner-Cremer[5], Thomas Wonik[34], Xiaosen Zhang[35]

[1]Institute of Geology and Mineralogy, University of Cologne, Cologne, Germany.

[2]Institute of Geological Sciences & Oeschger Centre for Climate Change Research, University of Bern, Bern, Switzerland.

[3]School of Earth, Atmospheric, and Life Science, University of Wollongong, Wollongong, Australia.

[4]International Pacific Research Center, University of Hawaii at Manoa, Honolulu, Hawaii, USA.

[5]Palaeoecology, Department of Physical Geography, Utrecht University, Utrecht, The Netherlands.

[6]National Environmental Isotope Facility, British Geological Survey, Nottingham, UK.

[7]Centre for Environmental Geochemistry, School of Biosciences, University of Nottingham, UK.

[8]Dipartimento di Scienze della Terra, University of Pisa, Pisa, Italy.

[9]Institute of Earth Sciences and Earth Resources-Italian National Research Council (IGG-CNR), Pisa, Italy.

[10]Dipartimento di Biologia Ambientale, Università di Roma "La Sapienza", Rome, Italy.

[11]Department of Animal Ecology & Systematics, Justus Liebig University Giessen, Giessen, Germany.

[12]Dipartimento di Scienze della Terra, Università di Firenze, Firenze, Italy.

[13]CNRS UMR 7194, Muséum National d'Histoire Naturelle, Institut de Paléontologie Humaine, Paris, France.

[14]Istituto di Geologia Ambientale e Geoingegneria – CNR, Rome, Italy.

[15]Faculty of Geology and Mineralogy, University of Tirana, Albania.

[16]School of Chemistry, University of Bristol, Bristol, UK.

[17]CNRS UMR 5554, Institut des Sciences de l'Evolution de Montpellier, Université de Montpellier, Montpellier, France.

[18]Fachbereich Geowissenschaften, Universität Bremen, Bremen, Germany.

[19]Faculty of Geology and Geoenvironment, National and Kapodistrian University of Athens, Athens, Greece.

[20]Paleoenvironmental Dynamics Group, Institute of Earth Sciences, Heidelberg University, Heidelberg, Germany.

[21]Institute of Geosciences, Christian-Albrechts-Universität zu Kiel, Kiel, Germany.

[22]Institute of Geosciences and Meteorology, University of Bonn, Bonn, Germany.

[23]University Ss Cyril and Methodius, Institute of Biology, Skopje, FYROM.

[24]Dipartimento di Scienze della Vita, Laboratorio di Palinologia e Paleobotanica, Università di Modena e Reggio Emilia, Modena, Italy.

[25]Laboratoire des Sciences du Climat et de l'Environnement, UMR 8212, CEA/CNRS/UVSQ et Université Paris-Saclay, Gif-Sur-Yvette, France.

[26]Helmholtz Centre Potsdam, GFZ German Research Centre for Geosciences, Potsdam, Germany.

[27]The Department of Geography, Geology and Environment, University of Hull, Hull, UK.

[28]Istituto Nazionale di Geofisica e Vulcanologia, Rome, Italy.

[29]Dipartimento di Scienze della Terra e Geoambientali, University of Bari, Bari, Italy.

[30]IDPA-CNR, Milan, Italy.

[31]Center for Climate Physics, Institute for Basic Science, Busan, South Korea

[32]Pusan National University, Busan, South Korea

[33]Dipartimento di Scienze della Vita, Laboratorio di Palinologia e Paleobotanica, Università di Modena e Reggio Emilia, Modena, Italy.

[34]Leibniz Institute for Applied Geophysics (LIAG), Hannover, Germany.

[35]Institute of Loess Plateau, Shanxi University, Taiyuan, China.

*Correspondence to: wagnerb@uni-koeln.de.

† these authors contributed equally to this work.

Mediterranean climates are characterized by strong seasonal contrasts between dry summers and wet winters. Changes in winter rainfall are critical, but difficult to simulate accurately[1] and reconstruct on Quaternary time-scales. This is partly because regional hydroclimate records covering multiple glacial-interglacial cycles[2,3] with different underlying orbital geometries, global ice volume, and atmospheric greenhouse gas concentrations are scarce. Moreover, the underlying mechanisms of change and their persistence remain to be explored. Here we show that, over the past 1.36 Myr, wet winters in the Northcentral Mediterranean tend to occur with high contrasts in local, seasonal insolation and a vigorous African summer monsoon. Our proxy time series from Lake Ohrid on the Balkan Peninsula, coupled to a 784-kyr-transient climate model hind cast, suggest that increased sea-surface temperatures amplify local cyclogenesis while also refuelling North Atlantic low pressure systems entering the Mediterranean during phases characterized by low continental ice volume and high atmospheric CO_2 concentrations. Comparison with modern reanalysis data shows that current drivers of rainfall amount in the Mediterranean share some similarities to those driving the reconstructed precipitation increases. Our extended record covers multiple insolation maxima and therefore is an important benchmark for testing climate model performance.

In the Mediterranean borderlands the amount and temporal extent of precipitation during the winter half-year (October to March) determines the prevailing type of vegetation and water availability for agrarian land use. In recent decades, reduction of winter precipitation has become a regular phenomenon in this region, with anthropogenic greenhouse gas (GHG) and aerosol forcing identified as potential contributors[4]. Current climate model simulations, using the Representative Concentration Pathway (RCP) 4.5 and 8.5 scenarios, predict a progressive summer drying over the next century[1]. Precipitation changes during the Northern Hemisphere

(NH) winter months are less well constrained, with different simulation runs showing trends both towards wetter and drier conditions. The uncertainty in winter precipitation projections limits the extent to which current modelling approaches are useful for decision makers[5,6].

Long-term, empirical baseline data are helpful to constrain uncertainties in climate modelling proxy records. Proxy records and modelling experiments suggest that enhanced precipitation in the Mediterranean region is in phase with the northward shift of the intertropical convergence zone (ITCZ) and increase in African monsoon strength during precession minima causing Northern Hemisphere summer insolation (NHSI) maxima and winter insolation (NHWI) minima[2,7,8,9]. However, most continental records that are capable of capturing hydroclimate change do not cover multiple NHSI maxima with different underlying orbital geometries. In fact, the majority of records are limited to the Holocene[10,11], yet the Early Holocene NHSI maximum was relatively weak compared to most other Quaternary interglacials, due to lower eccentricity. Terrestrial proxy time series covering multiple NHSI maxima from the Mediterranean region are scarce[2,3]. Sediment records from the Mediterranean Sea provide continuity throughout the Plio-Pleistocene and capture cessations of deep-water ventilation associated with the formation of prominent, organic-rich sapropel layers[12,13]. While multiple factors contribute to sapropel formation, increased freshwater input, particularly from the African continent during NHSI-forced monsoon maxima, is considered the most important[14,15]. Hence, the Mediterranean sapropel record is thought to be an excellent indicator of the relative timing of increased African monsoon strength rather than a direct indicator of precipitation in, and runoff from, the entirety of the Mediterranean realm. Reconstructed precipitation increases in the northern Mediterranean borderlands during sapropel formation have been interpreted to be a product both of intensified summer and winter precipitation[15,16]. Modelling experiments explain increased winter precipitation by stronger wintertime storm tracks[2] or air-sea temperature difference, and locally induced convective precipitation that dominate freshwater budget changes on obliquity time scales[17].

Alternatively, conceptual models based on proxy time series have suggested increases in the frequency and intensity of low pressure systems evolving in the Mediterranean region, mostly during fall and early winter[7,8,16]. Hence, a well-dated proxy record covering multiple glacial-interglacial cycles and being sensitive to changes in Mediterranean hydroclimate is key to addressing long-standing questions regarding the underlying mechanisms, timing, and amplitude of precipitation variability under different climate boundary conditions (GHG concentration, orbital geometries, continental ice sheet volume and extent).

Here, we assess precipitation variability in a continuous, independently dated 1.36-Myr sedimentary record from Lake Ohrid (Fig. 1, Extended Data Fig. 1). Climate variations at this site represent broader climate variability across the northern Mediterranean borderlands[18]. We compare our sedimentary proxy time series with transient climate simulation data and prominent monsoon records, to provide a mechanistic understanding of precipitation variability and seasonality, as well as phase relationships to orbital forcing.

Lake Ohrid is of tectonic origin and 293 m deep. The lake is hydrologically open and primarily fed by an extensive karst aquifer system, which supplies ions (mainly Ca^{2+} and HCO_3^-) to the lake and filters particulate matter[19]. Scientific drilling in 2013 resulted in a 584-m-long composite sediment succession from the lake centre, comprised of fine-grained hemi-pelagic muds in the upper 447 m[18,20]. Sedimentation is thought to have been uninterrupted, with no evidence of unconformities or erosion surfaces. Independent age control from 16 interspersed tephra layers in combination with magnetostratigraphy (Fig. 1, Extended Data Figs 2 and 3, Extended Data Table 1, Extended Data Table 2) provides a robust chronological framework. This framework allows us to match changes in orbital parameters with our proxy data to refine the age-depth relationships. The data demonstrate that the Lake Ohrid record spans the last 1.36 Myr (Fig. 1).

Indicators for detrital input (quartz, potassium), catchment vegetation (arboreal pollen excluding pine (AP-P), deciduous oaks), and hydrological variability (total inorganic carbon (TIC), Ca/K, $\delta^{18}O_{calcite}$, $\delta^{13}C_{calcite}$) show clear orbital-scale cyclicity, also characterized by a precessional (~21 ka) component (Fig. 2; Extended Data Figs 4, 5, and 6). The persistence of the orbital cyclicity in our data is widely unaffected by tectonic forcing on basin development and lake ontogeny (Extended Data Fig. 5). During periods of global ice volume minima and NHSI maxima, we observe prominent peaks in the hydrological and vegetation proxy data (Fig. 2). We interpret these peaks in TIC (mainly from endogenic calcite) and Ca/K (a proxy for the concentration of calcite) to result from enhanced activity of, and ion supply from, the karst aquifers combined with higher aquatic productivity due to warmer conditions[19]. Pollen show a simultaneous increase in vegetation cover, particularly deciduous oaks, during early phases of interglacials. Deciduous oaks benefit from a limited length of the summer dry season[21]. Lower $\delta^{13}C_{calcite}$ values during these periods suggest greater soil development, while lower $\delta^{18}O_{calcite}$ (Extended Data Fig. 4) indicate more positive precipitation/evaporation (P/E) balance[18]. Thus, aquatic and terrestrial datasets suggest higher temperatures along with maxima in annual precipitation amount and potential shorter summer aridity during interglacials (Extended Data Fig. 5).

To provide a better understanding of the observed precipitation variability from the Lake Ohrid record in a regional context, we analysed climate data time series derived from a transient 784-kyr simulation using the earth system model LOVECLIM[22,23] (Extended Data Fig. 7) as well as NOAA reanalysis precipitation data of the Lake Ohrid region for the time period 1979–2017. Temperature time series of the 5°x5° Lake Ohrid grid cell simulated by the LOVECLIM earth system model closely resemble records of first-order global ice volume (Extended Data Fig. 4), such as the LR04 benthic oxygen isotope stack[24] ($r=-0.8737$ or $r^2=0.76$ based on 1000-year averages of both data sets). The close match to changes in the amount of detrital siliciclastics and tree pollen (AP-P) confirms the sensitivity of the Lake

Ohrid record to global-scale climate fluctuations (Fig. 2; Extended Data Figs 4 and 5). The highest amplitudes in precipitation time series occur during phases of reduced ice volume, with prominent peaks during NHSI maxima. The significant positive relationship between simulated precipitation and our precipitation proxy time series (r^2=0.38), and the persistence of the relationship with orbital parameters (Extended Data Fig. 5), suggest that the local response recorded at Lake Ohrid also captures changes in regional hydroclimate back to 1.36 Ma (Fig. 2).

Seen both in paleo records and in climate model simulations, the intensification of NH monsoon systems during precession minima and NHSI maxima is a prominent example of orbital forcing on changes in precipitation variability[14,15,25]. Iconic records of monsoon strength, such as the Chinese speleothem[26], eastern Mediterranean sapropel[12,13,26] and planktonic foraminifera oxygen isotope records[14,15,27], show a positive phase relationship with Lake Ohrid hydrological proxy time series (Fig. 2). Strengthening of NH monsoons results from a northward displacement of atmospheric circulation systems, including the position of the Hadley cells and the ITCZ during NH summer. The shift of the Hadley cell amplifies subsidence over, and persistence of, high-pressure systems in the Mediterranean region, leading to warmer and drier summers[17], and higher sea surface temperatures (SST)[16,28]. Reduced NHWI has highest impact on tropical and subtropical latitudes[2] and leads to low latitude cooling and a southward shift of the ITCZ and the NH Hadley and Ferrel cells. Furthermore, this cooling results in a reduced meridional temperature gradient leading to a weakening of the westerlies based on the thermal wind relationship. The observed correspondence between the Lake Ohrid precipitation record (Fig. 2, Extended Data Figs 4 and 5) and the monsoon archives suggests increased precipitation during the winter half-year for this region when NHWI is low.

The Lake Ohrid record, in combination with the transient simulation time series and the NOAA reanalysis data, may provide fundamental insights into the mechanisms invoked by orbital forcing on Mediterranean precipitation. The monthly NOAA reanalysis data of the last 39 years show high precipitation anomalies (defined as above two standard deviations) to occur between the months of September and December (Extended Data Fig. 8). The atmospheric pattern associated with these precipitation events exhibits a trough in the Gulf of Genoa region (Extended Data Fig. 8), pointing to either increased cyclogenesis over or advection of North Atlantic low pressure into the western Mediterranean region.

The annual cycle of simulated Lake Ohrid precipitation in LOVECLIM is in good agreement with the reanalysis data; the model, however, underestimates the annual mean precipitation (Extended Data Fig. 8). Maxima in our simulated precipitation time series (defined as above two standard deviations) indicate a positive anomaly from September to November (SON) in agreement with the reanalysis data (Fig. 3, Extended Data Fig. 8). Despite important differences in the geographical expansion of geopotential height anomalies, both the NOAA and LOVECLIM data show pronounced troughs in the central Mediterranean area and an increase of rainfall during winter half-year in our focus region (Fig. 3). Our observations support previous modelling experiments suggesting that weakened atmospheric stratification and reduced hemispheric temperature contrasts[2], in combination with an increased contrast between warm SST and lower continental air temperatures[17], fuel precipitation increase in the Mediterranean. Such a preconditioning is particularly pronounced at the beginning of the fall, when the stronger thermal inertia of the sea relative to the land promotes local cyclogenesis[17,29]. Local cyclogenesis in combination with the southward shift in the NH atmospheric circulation cells during the winter half-year, which also favours a more southerly trajectory for storm tracks across the North Atlantic and into the Mediterranean[2], lead to increased winter rainfall in the Mediterranean mid-latitudes.

Owing to the significant positive correlation between the simulation and our proxy time series (Extended Data Fig. 5), in terms of timing and amplitude, we infer that this mechanism primarily controlled precipitation at Lake Ohrid for the last 1.36 Myr. Indeed, similar to the NH summer monsoon records, we observe a strong influence of NHSI and a reduced winter temperature contrast in the NH throughout the entirety of our multiproxy time series, suggesting persistence of the mechanism during different climate boundary conditions. The positive phase relationship between the Lake Ohrid precipitation proxy time series and sapropel records (Fig. 2) indicates a strong coherence of African summer monsoon strength and widespread Mediterranean winter half-year precipitation. Some peaks in our precipitation proxy time series, which are not represented by sapropel layers (Fig. 2), may indicate lower monsoon strength and reduced runoff from the African continent or that the general setting required for sapropel deposition and preservation was not established in the Mediterranean Sea during these periods[15]. During colder and drier glacial periods[3] with increased global ice volume, lower atmospheric CO_2 concentrations, and stronger mid-latitude westerlies, insolation forcing on precipitation appears suppressed in our record. This is in agreement with the sensitivity simulations conducted to disentangle the individual effects of orbital forcing, NH ice sheets, and CO_2 on Lake Ohrid precipitation (Extended Data Fig. 7).

Precessional forcing on insolation is not only the key driver of the NH monsoons, it also exerts a strong control on precipitation variability in the Mediterranean mid-latitudes during the Quaternary. Lake Ohrid sediment cores record highly resolved and chronologically well-constrained information on precipitation maxima during phases of lower intrahemispheric temperature contrast and peak SST's over the last 1.36 Myr. The apparent equivalence of the past regional key drivers of precipitation extremes to those produced by continued anthropogenic increase of atmospheric GHG concentrations may help to reduce simulation uncertainties and makes these results also relevant to predictions for the future evolution of Mediterranean climate.

References:

1. IPCC, 2013: Annex I: Atlas of Global and Regional Climate Projections [van Oldenborgh, G. J., M. Collins, J. Arblaster, J. H. Christensen, J. Marotzke, S. B. Power, M. Rummukainen and T. Zhou (eds.)]. In: Climate Change 2013: The Physical Sci¬ence Basis. Contribution of Working Group I to the Fifth Assessment Report of the Intergovernmental Panel on Climate Change [Stocker, T. F., D. Qin, G.-K. Plattner, M. Tignor, S. K. Allen, J. Boschung, A. Nauels, Y. Xia, V. Bex and P. M. Midgley (eds.)]. Cambridge University Press, Cambridge, United Kingdom and New York, NY, USA (2013).

2. Kutzbach, J. E., Chen, G., Cheng, H., Edwards, R. & Liu, Z. Potential role of winter rainfall in explaining increased moisture in the Mediterranean and Middle East during periods of maximum orbitally-forced insolation seasonality. *Clim. Dyn.* **42**, 1079−1095 (2014). doi:10.1007/s00382-013-1692-1

3. Tzedakis, P. C., Hooghiemstra, H. & Pälike H. The last 1.35 million years at Tenaghi Philippon, revised chronostratigraphy and long-term vegetation trends. *Quat. Sci. Rev.* **25,** 3416−3430 (2006). doi:10.1016/j.quascirev.2006.09.002

4. Hoerling, M. et al. On the increased frequency of Mediterranean drought. *J. Climate* **25**, 2146−2161 (2012). doi:10.1175/JCLI-D-11-00296.1

5. Weisheimer, A. & Palmer, T. N. On the reliability of seasonal climate forecasts. *J. Royal Soc., Interface* **11**, 20131162 (2014). doi.org/10.1098/rsif.2013.1162

6. Totz, S., Tziperman, E., Coumou, D., Pfeiffer, K. & Cohen, J. Winter Precipitation Forecast in the European and Mediterranean Regions Using Cluster Analysis. *Geophys. Res. Lett.* **44**, 12,418–12,426 (2017). doi.org/10.1002/2017GL075674

7. Milner, A. M. et al. Enhanced seasonality of precipitation in the Mediterranean during the early part of the Last Interglacial. *Geology* **40**, 919−922 (2012). doi:10.1130/G33204.1

8. Toucanne, S. et al. Tracking rainfall in the northern Mediterranean borderlands during sapropel deposition. *Quat. Sci. Rev.* **129**, 178−195 (2015). doi:10.1016/j.quascirev.2015.10.016

9. Stockhecke, M. et al. Millennial to orbital-scale variations of drought intensity in the Eastern Mediterranean. *Quat. Sci. Rev.* **133**, 77−95 (2016). doi: 10.1016/ j.quascirev.2015.12.016

10. Roberts, N. et al. Stable isotope records of Late Quaternary climate and hydrology from Mediterranean lakes: the ISOMED synthesis. *Quat. Sci. Rev.* **27**, 2426−2441 (2008). doi:10.1016/j.quascirev.2008.09.005

11. Magny, M. et al. North–south palaeohydrological contrasts in the central Mediterranean during the Holocene: tentative synthesis and working hypotheses. *Clim. Past* **9**, 2043−2071 (2013). doi:10.5194/cp-9-2043-2013

12. Emeis K.-C., Camerlenghi A., McKenzie J. A., Rio D.& Sprovieri R., The occurrence and significance of Pleistocene and Upper Pliocene sapropels in the Tyrrhenian Sea. *Mar. Geol.* **100**, 155−182 (1991). doi:10.1016/0025-3227(91)90231-R

13. Kroon, D. al. Oxygen isotope and sapropel stratigraphy in the Eastern Mediterranean during the last 3.2 million years, in *Proceedings of the Ocean Drilling Program. Scientific results***,** A. H. F. Robertson, K.-C. Emeis, C. Richter, A. Camerlenghi. Eds. (College Station, Texas, 1998), vol. 160, pp 181−190 (1998).

14. Rossignol-Strick, M. Mediterranean Quaternary sapropels, an immediate response of the African monsoon to variation of insolation. *Palaeogeogr. Palaeoclimatol. Palaeoecol.* **49**, 237−263 (1985). doi:10.1016/0031-0182(85)90056-2

15. Rohling, E. J., Marino, G. & Grant, K. M. Mediterranean climate and oceanography, and the periodic development of anoxic events (sapropels). *Earth Sci. Rev*. **143**, 62−97 (2015). doi:10.1016/j.earscirev.2015.01.008

16. Tzedakis, P. C. Seven ambiguities in the Mediterranean palaeoenvironmental narrative. *Quat. Sci. Rev*. **26**, 2042−2066 (2007). doi:10.1016/j.quascirev.2007.03.014

17. Bosmans, J. H. C. et al. Precession and obliquity forcing of the freshwater budget over the Mediterranean. *Quat. Sci. Rev.*, **123**, 16−30 (2015). doi:10.1016/j.quascirev.2015.06.008

18. Wagner, B. et al. The environmental and evolutionary history of Lake Ohrid (FYROM/Albania): Interim results from the SCOPSCO deep drilling project. *Biogeosciences* **14**, 2033−2054 (2017). doi:10.5194/bg-14-2033-2017

19. Vogel, H., Wagner, B., Zanchetta, G., Sulpizio, R. & Rosén, P. A paleoclimate record with tephrochronological age control for the last glacial-interglacial cycle from Lake Ohrid, Albania and Macedonia. *J. Paleolimnol.* **44**, 295−310 (2010). doi:10.1007/s10933-009-9404-x

20. Francke, A. et al. Sedimentological processes and environmental variability at Lake Ohrid (Macedonia, Albania) between 637 ka and the present. *Biogeosciences* **13**, 1179−1196 (2016). doi:10.5194/bg-13-1179-2016

21. Forner, A. et al. Extreme droughts affecting Mediterranean tree species' growth and water-use efficiency: the importance of timing. *Tree Physiol.* **38**, 1127−1137 (2018). doi:10.1093/treephys/tpy022

22. Friedrich, T., Timmermann, A., Tigchelaar, M., Timm, O. E. & Ganopolski, A. Nonlinear climate sensitivity and its implications for future greenhouse warming. *Sci. Adv*. **2** (2016), p. e1501923. doi:10.1126/sciadv.1501923

23. Timmermann, A. & Friedrich, T. Late Pleistocene climate drivers of early human migration. *Nature* **538**, 92−95 (2016). doi:10.1038/nature19365

24. Lisiecki, L. E. & Raymo, M. E. A Pliocene-Pleistocene stack of 57 globally distributed benthic $\delta^{18}O$ records. *Paleoceanography* **20**, PA1003 (2005). doi:10.1029/2004PA001071

25. Cheng, H. et al. The Asian monsoon over the past 640,000 years and ice age terminations. *Nature* **534**, 640−646 (2016). doi:10.1038/nature18591

26. Konijnendijk, T. Y. M., Ziegler, M. & Lourens, L. J. Chronological constraints on Pleistocene sapropel depositions from high-resolution geochemical records of ODP Sites 967 and 968. *Newslett. Stratigr.* **47**, 263−282 (2014). doi:10.1127/0078-0421/2014/0047

27. Colleoni, F., Masina, S., Negri, A. & Marzocchi, A. Plio–Pleistocene high–low latitude climate interplay: a Mediterranean point of view. *Earth Planet. Sci. Lett.* **319–320,** 35−44 (2012). doi:10.1016/j.epsl.2011.12.020

28. Martrat, B., Jimenez-Amat, P., Zahn, R. & Grimalt J. O., Similarities and dissimilarities between the last two deglaciations and interglaciations in the North Atlantic region. *Quat. Sci. Rev.* **99**, 122−134 (2014). doi:10.1016/j.quascirev.2014.06.016

29. Trigo, R. M., Osborne, T. J. & Corte-Real, J. M. The North Atlantic Oscillation influence on Europe: climate impacts and associated physical mechanisms. *Clim. Res*. **20**, 9−17 (2002). doi:10.3354/cr020009

30. Laskar, J. et al. A long-term numerical solution for the insolation quantities of the earth. *Astron. Astrophys*. **428**, 261−285 (2004). doi:10.1051/0004-6361:20041335

Acknowledgments: The Hydrobiological Institute in Ohrid (S. Trajanovski and G. Kostoski) and the Hydrometeorological Institute in Tirana (M. Sanxhaku and B. Lushaj) provided logistic support for site surveys and the scientific drilling campaign. Drilling was carried out by Drilling, Observation and Sampling of the Earth's Continental Crust (DOSECC). A. Skinner provided logistic and technical advice prior and during drilling operation. The Scientific Collaboration on Past Speciation Conditions in Lake Ohrid (SCOPSCO) drilling project was funded by the International Continental Scientific Drilling Program (ICDP), the German Ministry of Higher Education and Research, the German Research Foundation, the University of Cologne, the British Geological Survey, the INGV and CNR (both Italy), and the governments of the republics of North Macedonia and Albania. V. Scao collected the V5 tephra, which was $^{40}Ar/^{39}Ar$ dated with funding from LEFE "INTERMED" grant (CNRS-INSU) to S. Nomade.

Author Contributions: B Wagner and H Vogel designed the study and contributed equally. BW initiated and coordinated the SCOPSCO drilling project and drilling campaign. HV conceived major scientific ideas of this study. A Francke (sedimentology, chronology), T Friedrich (LOVECLIM modelling), T Donders (palynology), J Lacey (isotope geochemistry), and L Sadori (palynology) contributed and oversaw key datasets used in the study. They coordinated together with F Cremer-Wagner, M Leng, E Regattieri, T Wilke and G Zanchetta discussion and interpretations of proxy data groups and model results. Specific data were provided by A Bertini (pollen, MIS 19–21, MIS 25–28, MIS 42–43), N Combourieu-Nebout (pollen, MIS 1–4, MIS 8, MIS 14–15), B Giaccio (tephrostratigraphy), S Joannin (pollen, MIS 1–4, MIS 13–16, MIS 30), J Just (paleomagnetic data), K Kouli (pollen, MIS 6–8, MIS 10, MIS 16–19, MIS 28–30, MIS 33), I Kousis (pollen, MIS 11–12, MIS 15), A Koutsodendris (pollen, MIS 11–12, MIS 15), M Lagos (trace elements), N Leicher

(tephrostratigraphy), A Masi (pollen, MIS 5–6, MIS 20–25, MIS 31–32), A M Mercuri (pollen, MIS 6, MIS 34), S Nomade (tephrochronology), N Nowaczyk (paleomagnetic data), K Panagiotopoulos (pollen, MIS 7–8, MIS 35–43), O Peyron (pollen, MIS 1–4, MIS 13–16, MIS 30), L Sagnotti (paleomagnetic data), G Sinopoli (pollen, MIS 5–6), R Sulpizio (tephrostratigraphy) and P Torri (pollen MIS 6, MIS 34). S Krastel, K Lindhorst, and T Wonik coordinated the seismic survey of Lake Ohrid, the selection of the coring location and the geophysical measurements needed for core correlation. A Grazhdani, M Melles, J Reed, and Z Levkov contributed to the conception of the work. A Cvetkoska, J Holtvoeth, E Jovanvoska, S Tofilovska, and X Zhang provided micropaleontological and organic geochemistry data, which confirmed that the sediment succession from the DEEP site covers the entire history of Lake Ohrid. A Timmermann provided model infrastructure and resources. All authors contributed to the discussion and interpretation of the data and provided comments and suggestions to the manuscript.

Author Information: Reprints and permissions information is available at www.nature.com/reprints. Authors declare no competing interests. Correspondence and requests for materials should be addressed to wagnerb@uni-koeln.de. Data are available in the Pangaea database at https://doi.pangaea.de/10.1594/PANGAEA.896848, where links to the individual data sets are provided. Data used for LOVECLIM are available at https://climatedata.ibs.re.kr/grav/data/loveclim-784k.

Figure legends:

Fig. 1. Chronology and location of the Lake Ohrid DEEP site record. (a) The age model is based on tephrostratigraphic correlation of 16 tephra layers to their radiometrically dated proximal deposits (red, first-order tie points; ages and errors in Extended Data Table 1), **(b)**

tuning of total organic carbon (TOC) minima in the DEEP site record vs. inflection points in insolation and winter season length (green, second-order tie points; error of ±2,000 years), and cross evaluation of two paleomagnetic age reversals (a; dashed lines). The age modelling followed the methodological approach described in [20] (see Methods). **(c)** Location of Lake Ohrid and the approximate position of the intertropical convergence zone (ITCZ) in summer and winter.

Fig. 2. Lake Ohrid precipitation indicators and global monsoon records for the last 1.4 million years. **(a)** Eastern Mediterranean (EM) Sapropel ages[12,13,27], solid yellow lines indicate good and dashed yellow lines indicate poor/no match with the Ohrid reconstructions; **(b)** Chinese Speleostack $\delta^{18}O$ [26] in ‰ relative to VPDB; **(c)** Medstack $\delta^{18}O$ planktonic[28] in ‰ relative to VPDB; SST=sea-surface temperature, SSS=sea-surface salinity; **(d)** Lake Ohrid $\delta^{13}C$ endogenic calcite in ‰ relative to VPDB; **(e)** Lake Ohrid deciduous oaks pollen percentage; **(f)** Lake Ohrid total inorganic carbon (TIC) concentrations; **(g)** Northern Hemisphere winter insolation difference between the tropic of cancer and the arctic circle[30]; **(h)** annual mean precipitation amount for the Lake Ohrid grid cell from the LOVECLIM simulation; **(i)** Lake Ohrid arboreal pollen excluding *Pinus* pollen (AP-P) percentages. Tenaghi Philippon arboreal pollen (AP) percentages[3] **(k)** and LR04 benthic $\delta^{18}O$ stack[25] in ‰ relative to VPDB with odd numbers for interglacials **(l)** are shown for comparison. Red and white diamonds indicate the position of radiometrically dated tephra layers, blue and white diamonds the position of reversals of Earth’s magnetic field in the Lake Ohrid sediment record.

Fig. 3. Simulated Lake Ohrid precipitation and atmospheric anomaly pattern associated with precipitation maxima. (a) Simulated precipitation (cm yr^{-1}) for the Lake Ohrid grid cell. Data based on 1,000-year averages. Dashed line indicates two standard deviations above the mean. Red shading highlights precipitation values exceeding two standard deviations. See

Methods for details on the model simulations. **(b)** Composite anomalies of September-November (SON), 800 hPa geopotential height (m, shading) and wind (m s^{-1}, vectors) associated with precipitation maxima shown in (a).

Methods:

Lake and lake hydrology

Lake Ohrid (41°02’N, 20°43’E, 693 m a.s.l.; Fig. 1c) is located in the sub-Mediterranean climate zone with average monthly air temperatures between +26°C during summer and -1°C during winter. Precipitation in the Lake Ohrid watershed increases from 698 to 1,194 mm yr^{-1} with increasing altitude and occurs primarily during winter[31]. The lake is ~30 km long, ~15 km wide, and has a maximum water depth of 293 m (Extended Data Fig. 1). Sublacustrine karst springs (55%), direct precipitation, and river inflow (45%) constitute the water input. Due to an oligotrophic state, bottom waters remain partly oxygenated for several years, although the lake is oligomictic and a complete overturn occurs only every few years at present[32].

Sediment cores

Sediment cores from the Lake Ohrid DEEP site were recovered in spring 2013, using the Deep Lake Drilling System (DLDS) of Drilling, Observation and Sampling of the Earth’s Continental Crust (DOSECC) and within the framework of the multinational and interdisciplinary Scientific Collaboration on Past Speciation Conditions in Lake Ohrid (SCOPSCO) project that was co-sponsored by the International Continental Scientific Drilling Program (ICDP). The composite sediment record is based on 6 parallel boreholes that reached a terminal depth of 568 m[33]. Sediment recovery from 0 to 456.1 m composite depth (mcd) is 99.8%. Small gaps occur between 204.719 and 204.804 mcd (8.5 cm) and between 447.89 and 448.19 mcd (30 cm)[33]. Mass movement deposits (<3 cm) occur between 117 and 107 mcd, and between 55 and 50 mcd. Subsampling in the upper 447.12 mcd excluded mass movement and tephra deposits.

Scanning-X-ray fluorescence (XRF) analysis

Scanning-XRF analysis was performed at the University of Cologne, Germany, on split core surfaces at 2.5 mm increments and 10 s dwell time using an ITRAX XRF core scanner (Cox Analytics) equipped with an energy dispersive silicon drift detector and a Cr-tube set to 30 kV/30 mA. Raw data were processed and element-specific photon energy peaks were integrated in Q-spec (Cox Analytics).

Elemental analysis

Elemental analysis was performed on 16-cm-spaced samples (2794 samples, ~480 yr) following freeze-drying and homogenization at the University of Cologne. For total carbon (TC) and total inorganic carbon (TIC) measurements, an aliquot of 40 mg of the homogenized sample material was dispersed in 10 ml deionized water. TC was determined at combustion of 900°C and TIC was measured after treatment with 40% H_3PO_4 at 160°C using a DIMATOC 100 and a DIMATOC 200 (DIMATEC Corp., Germany). The total organic carbon (TOC) content was calculated by subtracting TIC from TC.

Fourier Transform Infrared Spectroscopy (FTIRS)

Relative concentration changes for quartz were assessed using FTIRS, on samples spaced at 32 cm (1462 samples, ~1,000 yr). Measurements were performed using a Bruker Vertex 70 equipped with a lN_2-cooled MCT (mercury-cadmium-telluride) detector, a KBr beam splitter, and a HTS-XT accessory unit (multisampler) in an air-conditioned laboratory at the University of Bern, Switzerland. 11 mg of each sample and 500 mg of oven-dried spectroscopic grade KBr (Uvasol®, Merck Corp.) were homogenized and scanned 64 times at a resolution of 4 cm^{-1} (reciprocal centimetres) for the wavenumber range from 3,750 to 520 cm^{-1} in diffuse reflectance mode. Data processing encompassed a linear baseline correction to remove baseline shifts and tilts by setting two points of the recorded spectrum to zero (3,750 and 2,210–2,200 cm^{-1}). Peak areas diagnostic for symmetric stretching of SiO_4 in quartz (778 and 798 cm^{-1}), and representative for relative abundance[34,35] were integrated using the OPUS (Bruker Corp.) software package.

Palynology processing and analysis

Pollen analysis was spaced at 64 cm (697 samples, ~2000 yr) following processing, identification, and counting approaches as described in[36]. Dry sediment (1.0–1.5 g) samples were treated with cold HCl (37%vol), cold HF (40%vol), and hot NaOH (10%vol) to dissolve carbonates, silicates, and humic acids, respectively. Glycerin-mounted residues were analysed by transmitted light microscopy to a mean of ~533 (incl. *Pinus*) and ~250 (excl. *Pinus*) grains/sample. Relative abundances are based on the total terrestrial pollen sum excl. *Pinus* due to overrepresentation and potential long-distance transport of this taxon[36]. Deciduous oak abundances represent the combined percentages of *Quercus robur* and *Q. cerris* types[37], which is commonly used as an indicator for mid-elevation, relatively humid forest across the Mediterranean[38,39,40,41].

Isotope analysis

Oxygen and carbon isotopes were analysed on bulk carbonate (calcite)[42] in samples spaced at 16 cm through zones of higher TIC (>0.5%), comprising a total of 1309 sediment samples. The samples were immersed in 5% NaClO solution for 24 h to gently disaggregate the sediment and oxidize reactive organic material. Potential biogenic carbonate was removed by sieving and the <64 µm fraction washed with deionized water, dried at 40°C, and then ground to a fine powder in an agate mortar. CO_2 was evolved from 10 mg $CaCO_3$ powders by reaction with anhydrous H_3PO_4 overnight inside a vacuum at a constant temperature of 25°C. The liberated CO_2 was cryogenically purified under vacuum and collected for analysis on a VG Optima dual inlet mass spectrometer. Oxygen and carbon isotope values are reported in standard delta notation ($\delta^{18}O_{calcite}$ and $\delta^{13}C_{calcite}$, respectively) in per mille (‰) calculated to the Vienna Pee Dee Belemnite (VPDB) scale using a within-run laboratory standard (MCS) calibrated against international NBS standards. Analytical reproducibility for the within-run standard was <0.1‰ (±1σ) for $\delta^{18}O$ and $\delta^{13}C$.

Magnetostratigraphic analyses

Remanent magnetization in its natural state (NRM) and after step-wise alternating field demagnetization (10 steps up to 100 mT) was measured on ~900 discrete cube (6.3 cm^3) samples with an average 48-cm-spacing at the Paleomagnetic Laboratory at the GeoForschungsZentrum, Potsdam, Germany, using a 2G Enterprises cryogenic magnetometer. Paleomagnetic directions (declination and inclination) were calculated using principle component analysis (PCA) after removal of low-coercivity magnetic overprints. After identification of geomagnetic polarity transitions, ~500 additional samples were taken at 2 to 3-cm-spacing across these transitions for high-resolution analysis at the Istituto Nazionale di Geofisica e Vulcanologia, Rome, Italy, using the same analytical set up and routine as in Potsdam. As glacial intervals of the core contain diagenetically formed greigite, which overprints the primary paleomagnetic signal[43], paleomagnetic transitions are faithfully preserved only in interglacial intervals, at the base of the Jaramillo sub-Chron (373.8 mcd) and at the Matuyama/Brunhes (M/B) boundary (287.6 mcd).

Tephrostratigraphic analysis

Eleven tephra and three cryptotephra layers have been identified in the upper 247 mcd of the record[44,45,46]. Two additional tephra layers from the lower (>247 mcd) part of the DEEP site record are introduced here. The tephrostratigraphic correlation of these tephras is based on geochemical fingerprinting of single glass shards using Wavelength Dispersive Electron Microprobe Analysis (WDS-EPMA) as described in [44].

Laser Ablation Inductively Coupled Plasma Mass Spectrometry (LA-ICP-MS) was used for trace element analyses on single glass shards of OH-DP-2669 and performed at the University of Bonn, Germany. The analyses were made with a Resonetics Resolution M50E 193 nm excimer laser ablation system coupled to a Thermo Scientific Element XR, using a spot size of 15-20 µm, a repetition rate of 5 Hz, and a count time of 35 s on the sample after 30 s on the gas blank (background). He (0.75 l min^{-1}) and Ar (~1.1 l min^{-1}) gas flow transported the ablated material via an in-house signal-smoothing device into the plasma of the ICP-MS. The signal was tuned to maximum intensity as well as stability at concurrently low oxide ratios (ThO/Th of ~0.0012) in order to minimize potentially interfering oxide species prior to analyses in low-resolution mode. Data reduction was performed using an in-house excel spreadsheet. Trace element concentrations were calculated via calibration against NIST612 using ^{29}Si as the internal standard (Si concentrations obtained by EPMA). Accuracies of the measurements were validated using reference glasses NIST610, T1-G, and ATHO-G.

$^{40}Ar/^{39}Ar$ dating was performed at the LSCE facility (CEA, UVSQ and University Paris-Saclay). V5 tephra (=OH-DP-2669 layer) was collected at the Montalbano-Jonico section (MJS; southern Italy, N40°17'32.8''; E16°33'27.4''). Twenty pristine sanidine crystals, of the fraction 0.6-1.0 mm, were extracted from V5 and irradiated for 2 h in the Cd-lined, in-core CLICIT facility of the Oregon State University TRIGA reactor (Irradiation CO 001). Subsequently, 14 crystals were individually loaded in a copper sample holder and put into a double vacuum Cleartran window. Each crystal was individually fused using a Synrad CO_2 laser at 10-15% of nominal power (~50 W). The extracted gas was purified for 10 min by two hot GP 110 and two GP 10 getters (ZrAl). Ar isotopes (^{36}Ar, ^{37}Ar, ^{38}Ar, ^{39}Ar, and ^{40}Ar) were analysed by mass spectrometry using a VG5400 equipped with an electron multiplier Balzers 217 SEV SEN coupled to an ion counter. Neutron fluence J for each sample is calculated using co-irradiated Alder Creek Sanidine (ACs-2) standard with an age of

1.1891Ma [47] and the total decay constant of [48]. J-values computed from standard grains is 0.00053220 ± 0.00000160. Mass discrimination was estimated by analysis of air pipette throughout the analytical period, and was relative to a $^{40}Ar/^{36}Ar$ ratio of 298.56 [49].

Tephra OH-DP-2669 is a 2.5 cm thick, yellowish layer with sharp upper and lower boundaries comprising up to 500 µm large platy glass shards and minor elongated micropumices. Its distinct trachytic composition (Extended Data Fig. 2) and the stratigraphic position between the M/B boundary (287.6 mcd) and OH-DP-2060 (Tufo di Bagni Albula, 524.84 ka [44]; Extended Data Table 1) narrow potential tephrostratigraphic equivalents. Tephra layer SC1-35.30/SUL2-1 from the Sulmona basin in the Italian Apennines is the only tephra with a similar trachytic composition[50,51] for this interval (Extended Data Fig. 2, Extended Data Table 2). SC1-35.30/SUL2-1 was correlated with tephra V5 from the MJS [52,53]. The majority of the SC1-35.30/SUL2-1 and OH-DP-2669 analyses correlate well with the more evolved group of V5 (V5b: SiO_2 >63% wt.; CaO <1.5% wt.) and only few analyses plot in the field of the less evolved group V5a (Extended Data Fig. 2, Extended Data Table 2). Trace element data of OH-DP-2669 and V5 [52] corroborate the correlation (Extended Data Fig. 3). Tephra layer SUL2-1 and V5 were $^{40}Ar/^{39}Ar$ dated at 722.8±2.4 ka[50] and 719.5±12.6 ka[53], respectively. The previous proposed correlation of SUL2-1/V5 with the Parmenide ash from the Crotone basin[50,52] is not considered here due to a slightly younger $^{40}Ar/^{39}Ar$ age of the Parmenide ash (710±5 ka) [54,55,56] and its geochemical differences to OH-DP-2669 (Extended Data Fig. 2, Extended Data Table 2).

Tephra OH-DP-2898 is a ~0.8 cm thick, whitish-yellowish band of lenses comprising fine-grained glass shards with a high degree of vesicularity and a phonolitic composition (Extended Data Fig. 2). It is located ~2 m below the M/B boundary, in calcareous sediments indicative for interglacial conditions[20]. The comparison of OH-DP-2898 glass composition with those of Sulmona tephra SUL2-19, -20, -25, -29 and -31 in a similar magnetostratigraphic position exclude a correlation (Extended Data Fig. 2). Other Sulmona tephra close to the M/B transition, SUL2-22, -23, and -27, have a composition similar to OH-DP-2898, but SUL2-23 has slightly lower alkali and higher CaO, FeO, TiO_2 concentrations (Extended Data Fig. 2, Extended Data Table 2). SUL2-27 is geochemically indistinguishable from OH-DP-2898, but deposited in glacial sediments of MIS 20 [57]. SUL2-22 is also geochemically indistinguishable from OH-DP-2898 and shares a similar stratigraphic position below the M/B boundary[58,59] and at the transition from MIS 20 to MIS 19 [57]. A correlation of OH-DP-2898 with tephra V4 from the MJS is not possible due to differences in the compositional range (Extended Data Fig. 2, Extended Data Table 2) and a younger ^{40}Ar/^{39}Ar age of 773.9±1.3 ka of V4 [52], quasi-synchronous position during the ^{10}Be peak or M/B transition[60]. Also a correlation of OH-DP-2898/SUL2-22 with tephra V3 of the MJS (801.2±19.5 ka) is excluded due to differences in the geochemical composition (Extended Data Fig. 2, Extended Data Table 2) and deposition of V3 during glacial conditions of MIS 20 [60]. The Pitagora ash from the Crotone basin is in a similar magneto- and climatostratigraphic position [55,61,62], but differs geochemically from OH-DP-2898/SUL2-22. Therefore, we regard a correlation of OH-DP-2898 with SUL2-22 as most robust and use its ^{40}Ar/^{39}Ar age of 791.9±1.9 ka [58] for our chronology.

In addition to the new tephra correlations, we updated ages for the upper tephra layers (Extended Data Table 1). This includes the Campanian Ignimbrite (Y-5/OH-DP-0169)[63] and tephra layers OH-DP-0404/POP2 and OH-DP-0435/X-6, based on new results from the Sulmona section[64]. The tephrostratigraphy of the Fucino record[65] improved and reassessed the correlations established for OH-DP-0617 and OH-DP-0624 [44]. The more precise ^{40}Ar/^{39}Ar age (158.8 ± 3.0 ka) of TF-17, which was correlated to OH-DP-0624, replaced the age of Vico B/OH-DP-0617 (162±6 ka)[66].

The correlation of cryptotephra OH-DP-1700.6 with the Vico β eruption[45] provided a new chronological tie-point at 410±2 ka [67]. The previously established correlation of tephra layer OH-DP-1955 with tephra layer SC-5 from the Mercure basin[44] was rejected in the light of its large uncertainty (±10.9 ka) and the new tephrostratigraphic data.

Reassessment of the raw Ar-isotope data of SC1-35.30/SUL2-1, the equivalent to OH-DP-2669, by updating the value of the atmospheric Ar-composition ($^{40}Ar/^{36}Ar$: 298.5 instead of 295.5 originally) and removing xenocrysts[58] yielded a new age of 715.02±5.4 ka (Extended Data Table 1) using the decay constant of [48] and an age of 1.1891 Ma for the ACs-2 flux standard[47]. Our new $^{40}Ar/^{39}Ar$ age of V5 (716.2±5.4 ka; MSWD = 0.8, P = 0.7) is indistinguishable within uncertainty and thus used for our chronology. All other $^{40}Ar/^{39}Ar$ were recalculated using the software ArAR[68] with a given decay constant and age for ACs-2 (1.1891 Ma)[47] and Fish Canyon sanidines (FCs) ages of 28.294 Ma[48].

Chronology

Following the methodological approach for the upper 247 mcd of the record[20], the chronology of the DEEP site sediment succession down to 447.12 mcd uses tephrochronological data[44,45,46] as 1st-order tie points. Tephrochronological data were used only where distinctive major element compositions (Extended Data Fig. 2, Extended Data Table 2) or trace element data sets (Extended Data Fig. 3) allow unambiguous tephrostratigraphic correlations. Trace element data sets of potential tephra equivalents are extremely rare for the period > 200 ka, thus limiting the applicability of this valuable tool.

Tuning of climate-sensitive proxy data (TOC; ~480 yr resolution) against orbital parameters was used as 2nd-order tie points considering that maxima in TIC represent interglacial periods[19,20]. Some chronologically well-constrained tephra layers deposited at the DEEP site since the penultimate glacial period (Y-5, X-6, P-11, and A11/12) occur at depths where TOC shows minima at times of the perihelion passage in March[20]. These perihelion passages in March correspond to the inflection points of increasing local summer insolation (21st June) and winter-season length (number of days between the September and March equinoxes) at the latitude of Lake Ohrid (41°N; Fig. 1). Increasing summer insolation promotes high summer temperatures, primary productivity in the water column, and increases organic matter (OM) supply to the sediments. An extended winter season improves lake-water mixing that enhances oxidation of OM in the water column and the surface sediments[20]. Thus, minima in TOC result from moderate OM supply to the sediments and improved oxidation of OM at the sediment surface and are used for tuning purposes.

The independent chronological information obtained from the 16 tephra and cryptotephra layers and 66 2nd-order tie points obtained from orbital tuning were cross evaluated by the two paleomagnetic age constraints (base of the Jaramillo sub-Chron and Matuyama/Brunhes M/B; Fig. 1). The age model was calculated using Bacon 2.2 [69], considering overall uniform (mem.strength=60, mem.mean=0.9, thick=80 cm) sedimentation rates (acc.shape=1.5, acc. mean=20) at the DEEP site[33]. An error of ±2,000 years was applied to the 2nd-order tie points to account for tuning inaccuracy. The 95% confidence intervals of ages for specific depths produced by the Bacon Bayesian age modelling average at ±5,500 years with a maximum of ±10,680 years. The resulting chronology implies that the upper 447.12 m of the DEEP site record covers the last 1.364 Myr, continuously.

We evaluated the DEEP site's chronology against the U/Th dated 0-160 ka Soreq Cave [20,70] and 185-250 ka Peqiin Cave speleothem[71] records and found agreement within errors of the chronologies. Arboreal pollen (AP) percentages in the DEEP site record are also in agreement with those from the orbitally-tuned Tenaghi Philippon record[3] back to 1.364 Ma (Fig. 2).

Model simulations and forcing

Transient simulations with the Earth system model LOVECLIM were conducted to study the impacts of orbital forcing, Northern Hemisphere (NH) ice sheets, and variations in atmospheric greenhouse gases (GHGs) on glacial-interglacial climate change.

LOVECLIM is a coupled ocean-atmosphere-sea ice-vegetation model[72]. The atmospheric component of LOVECLIM is the spectral T21, three-level model ECBilt[73] based on quasi-geostrophic equations extended by estimates of ageostrophic terms. The ocean-sea ice component of LOVECLIM consists of a free-surface Ocean General Circulation Model with a 3°x3° horizontal resolution coupled to a dynamic-thermodynamic sea-ice model[74]. Atmosphere and ocean components are coupled through the exchange of freshwater and heat fluxes. The model´s vegetation componentVECODE[75] computes the evolution of terrestrial vegetation cover based on annual mean surface temperature and precipitation.

The transient simulations of the last 784,000 years were forced by time-dependent boundary conditions for orbital parameters, atmospheric GHG concentrations, NH ice sheet orography, and albedo following the methodology described in[76]. The orbital forcing was calculated according to[77]. Atmospheric GHG concentrations were prescribed according to reconstructions from EPICA Dome C for CO_2[78] as well as CH_4 and N_2O[79]. Orbital forcing and atmospheric GHG concentrations were updated every model year. The effects of NH ice sheets on albedo and land topography were prescribed according to[80]. The forcing was applied with an acceleration factor of 5, which compresses 784,000 forcing years into 156,000 model years. This acceleration factor is appropriate for quickly equilibrating surface variables. The model simulation is an updated version of the one presented in[76] and uses a higher climate sensitivity resulting in a better representation of the glacial-interglacial surface temperature amplitude[23].

Four sensitivity simulations were conducted in addition to the full-forcing simulation described above (Extended Data Fig. 7). The sensitivity simulations cover the last four glacial cycles (408,000 years) and aim at exploring the individual effects of atmospheric GHGs, NH ice sheets and orbital parameters to glacial-interglacial climate change. The first sensitivity simulation uses transient forcing as described above but constant preindustrial (PI) atmospheric GHG concentrations. The "GHG effect" can then be calculated as the difference between the simulation using the full forcing and this simulation. The second sensitivity simulation uses transient forcing as described above but constant PI NH ice sheets (extent and albedo). The "NH ice sheet effect" is calculated as the difference between the full-forcing simulation and this simulation. Two simulations were designed to study the role of orbital forcing under warm and cold climate. For both simulations, transient orbital parameters are used. However, one simulation was run under constant PI atmospheric CO_2 concentration of 280 ppm, whereas the second simulation uses a constant atmospheric CO_2 concentration of 200 ppm resulting in a colder background climate.

Data analysis

To assess the temporal evolution of dominant periodicities in the DEEP site TIC and deciduous oak pollen percentage data, a wavelet power spectrum was computed for the respective time series. The time series were resampled at regular intervals (linear interpolation) at 0.3 kyr (TIC) and 1.0 kyr (pollen), and subsequently submitted to continuous wavelet transform (CWT, Morlet window) using PAST v.3.21 software[81] following the approach by [82]. Results of the CWT show clear 100 kyr orbital frequencies over the last 700 kyr, pronounced 41 kyr frequencies before that time and weak ~21 kyr orbital frequencies in the pollen record. Relative to the pollen, the CWT results of the TIC show a more pronounced 100 kyr cyclicity over the entire record, clear presence of 41 kyr periodicity in the early part of the record and very weak 21 kyr signals.

To quantitatively test the observed correlation between deciduous oak and TIC maxima against precession forcing, the bandpass-filtered 18–25 kyr component of the proxy data was regressed against precession based on the La2004 orbital solution[30].

Partial least squares regression (PLSR) was used to test the correlation of TIC and deciduous oaks as predictive variables with LOVECLIM temperature and precipitation output data. PLSR was performed using SIMCA 14 (Sartorius Stedim Biotech). All datasets were filtered using a frequency centred at 0.05 and a bandwidth of 0.02 prior to multivariate statistical analysis to accommodate for slight age offsets between proxy and simulation data.

We quantitatively assessed the relationships between sapropel occurrence (n = 53 for the last 1.4 Myr) and maxima in our Lake Ohrid precipitation proxies. For this we normalized both TIC and deciduous oak data to 1 and summed the data. Using a peak threshold of 0.5 in this dataset we defined mid-point ages for precipitation maxima (n = 93 for the last 1.36 Myr) and compared their timing to the closest sapropel mid-point ages. Thus, we were able to match 41 precipitation maxima to sapropel mid-point ages (mean age offset of 2.33 kyrs (SD = 1.68); solid yellow lines in Fig. 2). The 10 sapropels for which a match of the Ohrid precipitation signal is absent (dashed yellow lines in Fig. 2) are exclusively occurring within peak glacials.

Methods and Extended Data files references:

31. Popovska, C. & Bonacci, O. Basic data on the hydrology of Lakes Ohrid and Prespa. *Hydrol. Process*. **21**, 658–664 (2007). doi:10.1002/hyp.6252

32. Matzinger, A., Spirkovski, Z., Patceva, S. & Wüest A. Sensitivity of ancient Lake Ohrid to local anthropogenic impacts and global warming, *J. Great Lakes Res*. **32**, 158–179 (2006). doi:10.3394/0380-1330(2006)32[158:SOALOT]2.0.CO;2

33. Wagner, B. et al. The SCOPSCO drilling project recovers more than 1.2 million years of history from Lake Ohrid. *Sci. Drill*. **17**, 19–29 (2014). doi:10.5194/sd-17-19-2014

34. Farmer, V. C. The infrared spectra of minerals, edited by: V. C. Farmer, Mineralogical Society Monograph 4, 227 pp, Adlard & Son, Dorking, Surrey, (1974).

35. Chukanov, N. V. *Infrared Spectra of Mineral Species*. Springer, Dordrecht, Heidelberg, New York, London (2014). doi:10.1007/978-94-007-7128-4

36. Sadori, L. et al. Pollen-based paleoenvironmental and paleoclimatic change at Lake Ohrid (south-eastern Europe) during the past 500 ka. *Biogeosciences* **13**, 1423–1437 (2016). doi:10.5194/bg-13-1423-2016

37. Beug, H.-J. *Leitfaden der Pollenbestimmung für Mitteleuropa und angrenzende Gebiete.* Verlag Dr. Friedrich Pfeil, München, Germany (2004).

38. Cheddadi, R. et al. Imprints of glacial refugia in the modern genetic diversity of *Pinus sylvestris*. *Global Ecol. Biogeogr*. **15**, 271–282 (2006). doi:10.1111/j.1466-8238.2006.00226.x

39. Rossignol-Strick, M. The Holocene climatic optimum and pollen records of sapropel 1 in the Eastern Mediterranean, 9000–6000 BP. *Quat. Sci Rev*. **18**, 515–530 (1999). doi:10.1016/S0277-3791(98)00093-6

40. Langgut, D., Almogi-Labin, A., Bar-Matthews, M. & Weinstein-Evron, M. Vegetation and climate changes in the South Eastern Mediterranean during the Last Glacial–Interglacial cycle (86 ka): new marine pollen record. *Quat. Sci Rev*. **30**, 3960–3972 (2011). doi:10.1016/j.quascirev.2011.10.016

41. Combourieu-Nebout, N. et al. Climate changes in the central Mediterranean and Italian vegetation dynamics since the Pliocene. *Rev. Palaeobot. Palynol*. **218**, 127–147 (2015). doi:10.1016/j.revpalbo.2015.03.001

42. Lacey, J. H. et al. Northern Mediterranean climate since the Middle Pleistocene: a 637 ka stable isotope record from Lake Ohrid (Albania/Macedonia). *Biogeosciences* **13**, 1801−1820 (2016). doi:10.5194/bg-13-1801-2016

43. Just, J. et al. Environmental control on the occurrence of high-coercivity magnetic minerals and formation of iron sulfides in a 640 ka sediment sequence from Lake Ohrid (Balkans). *Biogeosciences* **13**, 2093–2109 (2016). doi:10.5194/bg-13-2093-2016

44. Leicher, N. et al. First tephrostratigraphic results of the DEEP site record from Lake Ohrid (Macedonia and Albania). *Biogeosciences* **13**, 2151–2178 (2016). doi:10.5194/bg-13-2151-2016

45. Kousis, I. et al. Centennial-scale vegetation dynamics and climate variability in SE Europe during Marine Isotope Stage 11 based on a pollen record from Lake Ohrid. *Quat. Sci. Rev*. **190**, 20−38 (2018). doi:10.1016/j.quascirev.2018.04.014

46. Francke, A. et al. Sediment residence time reveals Holocene shift from climatic to vegetation control on catchment erosion in the Balkans. *Global Planet. Change* **177**, 186–200. 2019. doi:10.1016/j.gloplacha.2019.04.005

47. Niespolo, E. M., Rutte, D., Deino, A. L. & Renne, P. R. Intercalibration and age of the Alder Creek sanidine $^{40}Ar/^{39}Ar$ standard. *Quat. Geochronol*. **39**, 205−213 (2017). doi:10.1016/j.quageo.2016.09.004

48. Renne, P. R., Balco, G., Ludwig, K. R., Mundil, R. & Min, K. Response to the comment by W. H. Schwarz et al. on "Joint determination of ^{40}K decay constants and $^{40}Ar*/^{40}K$ for the Fish Canyon sanidine standard, and improved accuracy for $^{40}Ar/^{39}Ar$ geochronology" by P. R. Renne et al. (2010). *Geochim. Cosmochim. Acta* **75**, 5097−5100 (2011). doi:10.1016/j.gca.2010.06.017

49. Lee, J. Y. et al. A redetermination of the isotopic abundances of atmospheric Ar. *Geochim. Cosmochim. Acta* **70**, 4507−4512 (2006). doi:10.1016/j.gca.2006.06.1563

50. Giaccio, B. et al. Revised Chronology of the Sulmona Lacustrine Succession, Central Italy. *J. Quat. Sci.* **28**, 545−551 (2013). doi:10.1002/jqs.2647

51. Giaccio, B. et al. Tephra layers from Holocene lake sediments of the Sulmona Basin, Central Italy: implications for volcanic activity in Peninsular Italy and tephrostratigraphy

in the Central Mediterranean area. *Quat. Sci. Rev*. **28**, 2710−2733 (2009). doi:10.1016/j.quascirev.2009.06.009

52. Petrosino, P. et al. The Montalbano Jonico marine succession: An archive for distal tephra layers at the Early–Middle Pleistocene boundary in southern Italy. *Quat. Internat*. **383**, 89−103 (2015). doi:10.1016/j.quaint.2014.10.049

53. Ciaranfi, N. et al. Integrated stratigraphy and astronomical tuning of Lower–Middle Pleistocene Montalbano Jonico section (Southern Italy). *Quat. Internat.* **219**, 109−120 (2010). doi:10.1016/j.quaint.2009.10.027

54. Massari, F. et al. Interplay between tectonics and glacio-eustasy: Pleistocene succession of the Crotone basin, Calabria (southern Italy). *Geol. Soc. Am. Bull*. **114**, 1183−1209 (2002). doi:10.1130/0016-7606(2002)114<1183:IBTAGE>2.0.CO;2

55. Capraro, L. et al. Climatic patterns revealed by pollen and oxygen isotope records across the Matuyama-Brunhes Boundary in the central Mediterranean (southern Italy). *Geol. Soc., London, Spec. Publ*. **247**, 159−182 (2005). doi:10.1144/GSL.SP.2005.247.01.09

56. Capraro, L. et al. Chronology of the Lower–Middle Pleistocene succession of the south-western part of the Crotone Basin (Calabria, Southern Italy). *Quat. Sci. Rev*. **30**, 1185−1200 (2011). doi:10.1016/j.quascirev.2011.02.008

57. Giaccio, B. et al. Duration and dynamics of the best orbital analogue to the present interglacial. *Geology* **43**, 603−606 (2015). doi:10.1130/G36677.1

58. Sagnotti, L. et al. Extremely rapid directional change during Matuyama-Brunhes geomagnetic polarity reversal. *Geophys. J. Internat*. **199**, 1110−1124 (2014). doi:10.1093/gji/ggu287

59. Sagnotti, L. et al. How fast was the Matuyama–Brunhes geomagnetic reversal? A new subcentennial record from the Sulmona Basin, central Italy. *Geophys. J. Internat.* **204**, 798−812 (2016). doi:10.1093/gji/ggv486

60. Simon, Q. et al. Authigenic ^{10}Be/^{9}Be ratio signature of the Matuyama–Brunhes boundary in the Montalbano Jonico marine succession. *Earth Planet. Sci. Lett.* **460**, 255−267 (2017). doi:10.1016/j.epsl.2016.11.052

61. Rio, D. et al. Reading Pleistocene eustasy in a tectonically active siliciclastic shelf setting (Crotone peninsula, southern Italy). *Geology* **24**, 743−746 (1996). doi:10.1130/0091-7613(1996)024<0743:RPEIAT>2.3.CO;2

62. Macri, P., Capraro, L., Ferretti, P. & Scarponi, D. A high-resolution record of the Matuyama-Brunhes transition from the Mediterranean region: The Valle di Manche section (Calabria, Southern Italy). *Phys. Earth Planet. Inter.* **278**, 1−15 (2018). doi:10.1016/j.pepi.2018.02.005

63. Giaccio, B., Hajdas, I., Isaia, R., Deino, A. & Nomade, S. High-precision ^{14}C and ^{40}Ar/^{39}Ar dating of the Campanian Ignimbrite (Y-5) reconciles the time-scales of climatic-cultural processes at 40 ka. *Sci. Rep.* **7**, 45940 (2017). doi:10.1038/srep45940

64. Regattieri, E., et al. A last Interglacial record of environmental changes from the Sulmona Basin (central Italy). *Palaeogeogr. Palaeoclimatol. Palaeoecol.* **472**, 51−66 (2017). doi:10.1016/j.palaeo.2017.02.013

65. Giaccio, B. et al. First integrated tephrochronological record for the last ~190 kyr from the Fucino Quaternary lacustrine succession, central Italy. *Quat. Sci. Rev.* **158**, 211−234 (2017). doi:10.1016/j.quascirev.2017.01.004

66. Laurenzi, M. A. & Villa, I. ^{40}Ar/^{39}Ar chronostratigraphy of Vico ignimbrites. *Period. Mineral.* **56**, 285−293 (1987)

67. Karner, D. B., Marra, F. & Renne, P. R. The history of the Monti Sabatini and Alban Hills volcanoes: groundwork for assessing volcanic-tectonic hazards for Rome. *J. Volcanol. Geotherm. Res.* **107**, 185−219 (2001). doi: 10.1016/S0377-0273(00)00258-4

68. Mercer, C. M. & Hodges, K.V. ArAR — A software tool to promote the robust comparison of K–Ar and $^{40}Ar/^{39}Ar$ dates published using different decay, isotopic, and monitor-age parameters. *Chem. Geol*. **440**, 148−163 (2016). doi:10.1016/j.chemgeo.2016.06.020

69. Blaauw, M. & Christen, J. A. Flexible paleoclimate age-depth models using an autoregressive gamma process. *Bayes. Analys*. **6**, 457−474 (2011). doi:10.1214/ba/1339616472

70. Grant, K. M. et al. Rapid coupling between ice volume and polar temperature over the past 150,000 years. *Nature* **491**, 744–747 (2012). doi:10.1038/nature11593

71. Bar-Matthews, M., Ayalon, A., Gilmour, M., Matthews, A. & Hawkesworth, C. J. Sea-land oxygen isotopic relationships from planktonic foraminifera and speleothems in the Eastern Mediterranean region and their implication for paleorainfall during interglacial intervals. *Geochim. Cosmochim. Acta* **67**, 3181−3199 (2003). doi:10.1016/S0016-7037(02)01031-1

72. Goosse, H. et al. Description of the Earth system model of intermediate complexity LOVECLIM version 1.2. *Geosci. Model Dev*. **3**, 603–633 (2010). doi:10.5194/gmd-3-603-2010

73. Opsteegh, J. D., Haarsma, R. J., Selten, F. M. & Kattenberg A. ECBILT: a dynamic alternative to mixed boundary conditions in ocean models. *Tellus, Ser. A, Dyn. Meterol. Oceanogr*. **50,** 348–367 (1998). doi:10.3402/tellusa.v50i3.14524

74. Goosse, H. & Fichefet, T. Importance of ice-ocean interactions for the global ocean circulation: A model study. *J. Geophys. Res*. **104**, 23337–23355 (1999). doi:10.1029/1999JC900215

75. Brovkin, V., Ganopolski, A. & Svirezhev, Y. A continuous climate-vegetation classification for use in climate-biosphere studies. *Ecol. Modell.* **101,** 251–261 (1997). doi:10.1016/S0304-3800(97)00049-5

76. Timmermann, A. et al. obliquity and CO_2 effects on Southern Hemisphere climate during the past 408 ka. *J. Clim*. **27**, 1863–1875 (2014). doi:10.1175/JCLI-D-13-00311.1

77. Berger, A. Long-term variations of daily insolation and Quaternary climate change. *J. Atmos. Sci*. **35**, 2362–2367 (1978). doi:10.1175/1520-0469(1978)035<2362:LTVODI>2.0.CO;2

78. Lüthi, D. et al. High-resolution carbon dioxide concentration record 650,000-800,000 years before present. *Nature* **453**, 379–382 (2008). doi:10.1038/nature06949

79. EPICA community members. Eight glacial cycles from an Antarctic ice core. *Nature* **429**, 623–628 (2004). doi:10.1038/nature02599

80. Ganopolski, A. & Calov, R. The role of orbital forcing, carbon dioxide and regolith in 100 kyr glacial cycles. *Clim. Past*, **7**, 1415–1425 (2011). doi:10.5194/cp-7-1415-2011

81. Hammer, O. PAleontological Statistics (PAST) Version 3.21 reference manual, Natural History Museum, University of Oslo (2018). https://folk.uio.no/ohammer/past/

82. Torrence, C. & Compo, G. P. A practical guide to wavelet analysis. *Bull. Am. Meteorol. Soc.* **79**, 61−78. (1998). doi:10.1175/1520-0477(1998)079<0061:APGTWA>2.0.CO;2

83. Lindhorst, K. et al. Sedimentary and tectonic evolution of Lake Ohrid (Macedonia/Albania). *Basin Res*. **27**, 84−101 (2015). doi:10.1111/bre.12063

84. Le Bas, M. J. Le Maitre, R. W. Streckeisen, A. & Zanettin, B. A Chemical Classification of Volcanic Rocks Based on the Total Alkali-Silica Diagram. *J. Petrol.* **27**, 745–750, (1986). doi:10.1093/petrology/27.3.745

85. Melard, G. Algorithm AS 197: A fast algorithm for the exact likelihood of autoregressive-moving average models. *Appl. Stat.* **33**,104–114 (1984). doi:10.2307/2347672

86. Zanchetta, G. et al. Aligning and synchronization of MIS5 proxy records from Lake Ohrid (FYROM) with independently dated Mediterranean archives: implications for DEEP core chronology. *Biogeosciences*, **13**, 2757–2768 (2016). doi:10.5194/bg-13-2757-2016

87. Wagner, B. et al. The last 40 ka tephrostratigraphic record of Lake Ohrid, Albania and Macedonia: a very distal archive for ash dispersal from Italian volcanoes. *J. Volcanol. Geotherm. Res.* **177**, 71–80 (2008). doi:10.1016/j.jvolgeores.2007.08.018.

88. Zanchetta, G. et al. Tephrostratigraphy, chronology and climatic events of the Mediterranean basin during the Holocene: An overview. *Holocene* **21**, 33–52 (2011). doi:10.1177/0959683610377531

89. Siani, G., Sulpizio, R., Paterne, M. & Sbrana, A. Tephrostratigraphy study for the last 18,000 C-14 years in a deep-sea sediment sequence for the South Adriatic. *Quat. Sci. Rev.* **23**, 2485–2500 (2004). doi:10.1016/j.quascirev.2004.06.004.

90. Albert, P. G. et al. Revisiting the Y-3 tephrostratigraphic marker: a new diagnostic glass geochemistry, age estimate, and details on its climatostratigraphical context, *Quat. Sci. Rev.* **118**, 105–121 (2015). doi:10.1016/j.quascirev.2014.04.002

91. Satow, C. et al. A new contribution to the Late Quaternary tephrostratigraphy of the Mediterranean: Aegean Sea core LC21, *Quat. Sci. Rev*. **117**, 96–112 (2015). doi:10.1016/j.quascirev.2015.04.005

92. Giaccio, B. et al. Isotopic (Sr-Nd) and major element fingerprinting of distal tephras: an application to the Middle-Late Pleistocene markers from the Colli Albani volcano, central Italy. *Quat. Sci. Rev*. **67**, 190–206 (2013). doi: 10.1016/j.quascirev.2013.01.028

93. Petrosino, P., Jicha, B. R., Mazzeo, F. C. & Russo Ermolli, E. A high resolution tephrochronological record of MIS 14–12 in the Southern Apennines (Acerno Basin, Italy). *J. Volcanol. Geotherm. Res*. **274**, 34–50 (2014). doi:10.1016/j.jvolgeores.2014.01.014

94. Marra, F., Karner, D. B., Freda, C., Gaeta, M. & Renne, P. Large mafic eruptions at Alban Hills Volcanic District (Central Italy): Chronostratigraphy, petrography and eruptive behavior. *J. Volcanol. Geotherm. Res*. **179**, 217–232 (2009). doi:10.1016/j.jvolgeores.2008.11.009

Data Availability

Data are available in the Pangaea database at https://doi.pangaea.de/10.1594/PANGAEA.896848, where links to the individual data sets are provided. Data used for LOVECLIM are available at https://climatedata.ibs.re.kr/grav/data/loveclim-784k.

Code Availability

Model data produced by the LOVECLIM simulations are available through the data centre of the IBS Center for Climate Physics: https://climatedata.ibs.re.kr/grav/data/loveclim-784k. Additional data are available upon request made to Tobias Friedrich (tobiasf@hawaii.edu).

Extended Data Legends

Extended Data Figure 1 | Map of Lake Ohrid and its surrounding area. Geology, topography, and bathymetry compiled from[19,83] and geological maps of Albania and North Macedonia. The lake is located at an altitude of 693 m a.s.l. and has a maximum water depth of 293 m. The water depth at the DEEP drill site is 240 m.

Extended Data Figure 2 | Correlation of tephra layers at the DEEP site with tephra layers from mid-distal records. Bi-oxide plots of **(a)** CaO vs. FeO_{total}, **(b)** CaO vs. Al_2O_3, **(c)** CaO vs. TiO_2, **(d)** Na_2O vs. K_2O, and **(e)** total alkali vs. silica (TAS) diagram[84] show the correlation of OH-DP-2669 with the tephra layers SC1-35.30/SUL2-1/V5 and the differences to the Parmenide ash. Bi-oxide plots of **(f)** CaO vs. FeO_{total}, **(g)** CaO vs. Al_2O_3, **(h)** CaO vs. TiO_2, **(i)** Na_2O vs. K_2O, and **(k)** TAS diagram show the correlation of OH-DP-2898 with tephra SUL2-22 and the differences to SUL2-23, -27, -31, V4, V3, and the Pitagora ash. Error bars of the Parmenide Ash indicate standard deviation[54]. Tephra ages, geochemical data, tephrostratigraphic discussion and references are provided in Extended Data Tables 1 and 2 and in Methods.

Extended Data Figure 3 | Correlation of tephra layers OH-DP-2669 and V5 based on trace element compositions. Trace element data of OH-DP-2669 support the correlation with tephra V5a/b[52]; (a) Th vs. Y, (b) Th vs. Zr, (c) Th vs. Nb, (d) Th vs.La, (e) Th vs. Ce, (f) Th vs. Pr, (g) Th vs. Nd, (h) Th vs.Gd, (i) Th vs.Yb. Error bars of OH-DP-2669 represent uncertainties at a 95% confidence interval.

Extended Data Figure 4 | Lake Ohrid LOVECLIM simulation data and sedimentary paleoclimate and paleoenvironment proxies. (a) Simulated surface-air temperature (SAT) for the Lake Ohrid grid cell from the LOVECLIM simulation; **(b)** simulated precipitation amount for the Lake Ohrid grid cell from the LOVECLIM simulation; **(c)** Lake Ohrid total organic carbon (TOC) concentrations; **(d)** Lake Ohrid $\delta^{13}C$ endogenic calcite in ‰ relative to VPDB; **(e)** Lake Ohrid $\delta^{18}O$ endogenic calcite in ‰ relative to VPDB; **(f)** Lake Ohrid relative sedimentary quartz content; **(g)** Lake Ohrid K intensities in kilo counts and displayed using a 11pt running mean; **(h)** Lake Ohrid ratio of Ca/K intensities displayed using a 11 pt running mean; **(i)** Lake Ohrid Ca intensities in kilo counts and displayed using a 11 pt running mean; **(k)** Lake Ohrid total inorganic carbon (TIC) concentrations; **(l)** Lake Ohrid deciduous oaks pollen percentages; **(m)** Lake Ohrid arboreal pollen excluding *Pinus* pollen (AP-P) percentages; red and white diamonds indicate the position of radiometrically dated tephra layers, blue and white diamonds the position of reversals of Earth's magnetic field in the Lake Ohrid sediment record. (b), (d), (e), (k), (l) and (m) are repeated from Fig. 2.

Extended Data Figure 5 | Data analysis. Continuous wavelet transform on % total inorganic carbon (TIC; **a**) and % deciduous oak pollen **(**DOP, **b)** from Ohrid DEEP (yellow=highest, red=lowest power, grey contour = cone of influence, black contour = 5% significance level [82] against red-noise background corrected for autocorrelation[81,85]). Least squares regression (red line) between band pass-filtered 18-25 kyr component of **(c)** % TIC and **(d)** the % DOP against precession at 1 kyr resolution. Blue lines indicate 95% bootstrapped (n=1999) confidence intervals. Significant negative responses to precession are seen in both proxies, with a stronger response in DOP. Partial datasets for the intervals <0.78Ma, <1.2Ma,

<1.36Ma are indicate persistence of the correlation despite changes in lake ontogeny and global scale changes in boundary conditions. Partial least squares regression (PLSR) using TIC and DOP as predictive variables and LOVECLIM **(e)** temperature and **(f)** precipitation simulations as observations demonstrate significant explanatory power by the proxies on the simulation time series, particularly for precipitation. PLSR was performed using SIMCA 14 (Sartorius Stedim Biotech), using 1.4-33 kyr bandpass filtered data to accommodate for slight age offsets between proxy and simulation data.

Extended Data Figure 6 | Lake Ohrid precipitation indicators and global monsoon records during MIS 5. (a) Ages of sapropels and humid phases in the Eastern Mediterranean based on Soreq Cave speleothem $\delta^{18}O$ data and U/Th chronology[71]; **(b)** simulated precipitation amount for the Lake Ohrid grid cell from the LOVECLIM simulation; **(c)** Lake Ohrid deciduous oaks pollen percentage; **(d)** Lake Ohrid total inorganic carbon (TIC) concentrations; **(e)** Chinese Speleostack $\delta^{18}O$ [25] in ‰ relative to VPDB; red and white diamonds indicate the position of radiometrically dated tephra layers in the Lake Ohrid record. The chronology of the MIS 5 interval in the Lake Ohrid DEEP site record is based on [86].

Extended Data Figure 7 | Simulated Lake Ohrid precipitation for full-forcing run and sensitivity simulations. (a) Lake Ohrid precipitation (cm yr^{-1}) for full-forcing simulation (black) and a simulation using only orbital forcing under a warm background climate (red). **(b)** Black line as in (a) and a simulation using only orbital forcing under a cold background climate (blue). **(c)** Black line as in (a) and a simulation using full-forcing except for a constant preindustrial NH ice sheet. **(d)** Black line as in (a) and a simulation using full-forcing except for constant preindustrial GHG concentrations. Please note that the sensitivity simulations only cover the last 408 kyr. Please see Methods for details on the sensitivity simulations.

Extended Data Figure 8 | Mean seasonal cycle of Lake Ohrid precipitation - model simulation and NOAA reanalysis data. (a) Reconstructed precipitation (cm yr^{-1}) for the Lake Ohrid reanalysis grid cell. Data based on monthly means. Dashed line indicates two standard deviations above the mean. **(b)** Composite anomalies of 850 hPa geopotential height (m) associated with Lake Ohrid precipitation maxima shown in (a) and referring to the months shown in (c). **(c)** Monthly distribution of precipitation maxima shown in (a). **(d)** Mean seasonal cycle of simulated Lake Ohrid precipitation (cm yr^{-1}) for all model years (green) and model years with annual-mean precipitation exceeding two standard deviations (magenta). Please see also Fig. 3a. **(e)** Mean seasonal cycle of Lake Ohrid precipitation (cm yr^{-1}) derived from NOAA reanalysis data (blue) and simulated for the 1–0 kyr period (red). The annual means were removed for better comparison and are provided in the panel.

Extended Data Table 1 | Selected tephra layers from Lake Ohrid and their correlation with tephra layers of other records. $^{40}Ar/^{39}Ar$ ages from literature were recalculated using a decay constant[48] and Alder Creek sanidine (ACs-2) at 1.1891 Ma[47] or Fish Canyon sanidine (FCs) at 28.294 Ma[48]. Tephra ages in bold are used for age-depth modelling in Fig. 1. Age uncertainties (95% confidence interval) are provided according to the original reference (Reference age).

Extended Data Table 2 | Average compositions of OH-DP-2669 and OH-DP-2898 and potential equivalent correlations. Data of SUL2-1, SUL2-22, SUL2-23, SUL2-27 from [51]; SC1-35.50 from [50]; V5, V4, V3, Pitagora ash from [52] and the Parmenide ash from [54]. $\bar{x}$ = mean; S = standard deviation; n= number of analysis.

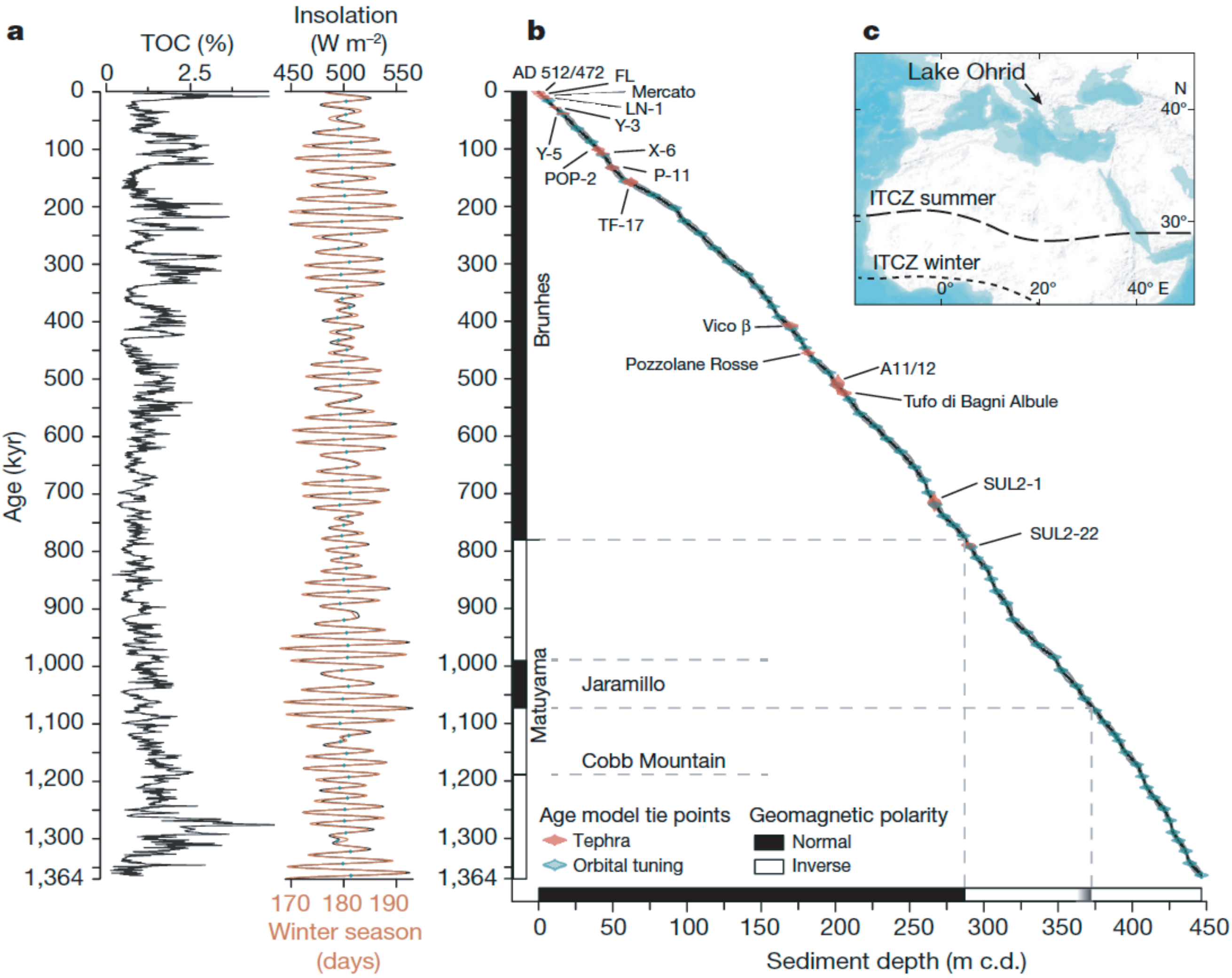
a
TOC (%)
Insolation (W m-2)
0
2.5
450
500
550
Age (kyr)
170 180 190
Winter season (days)
b
AD 512/472
FL
Mercato
LN-1
Y-3
Y-5
X-6
POP-2
P-11
TF-17
Vico β
Pozzolane Rosse
A11/12
Tufo di Bagni Albule
SUL2-1
SUL2-22
Brunhes
Matuyama
Jaramillo
Cobb Mountain
Age model tie points
Tephra
Orbital tuning
Geomagnetic polarity
Normal
Inverse
Sediment depth (m c.d.)
c
Lake Ohrid
ITCZ summer
ITCZ winter
N
40°
30°
0°
20°
40° E

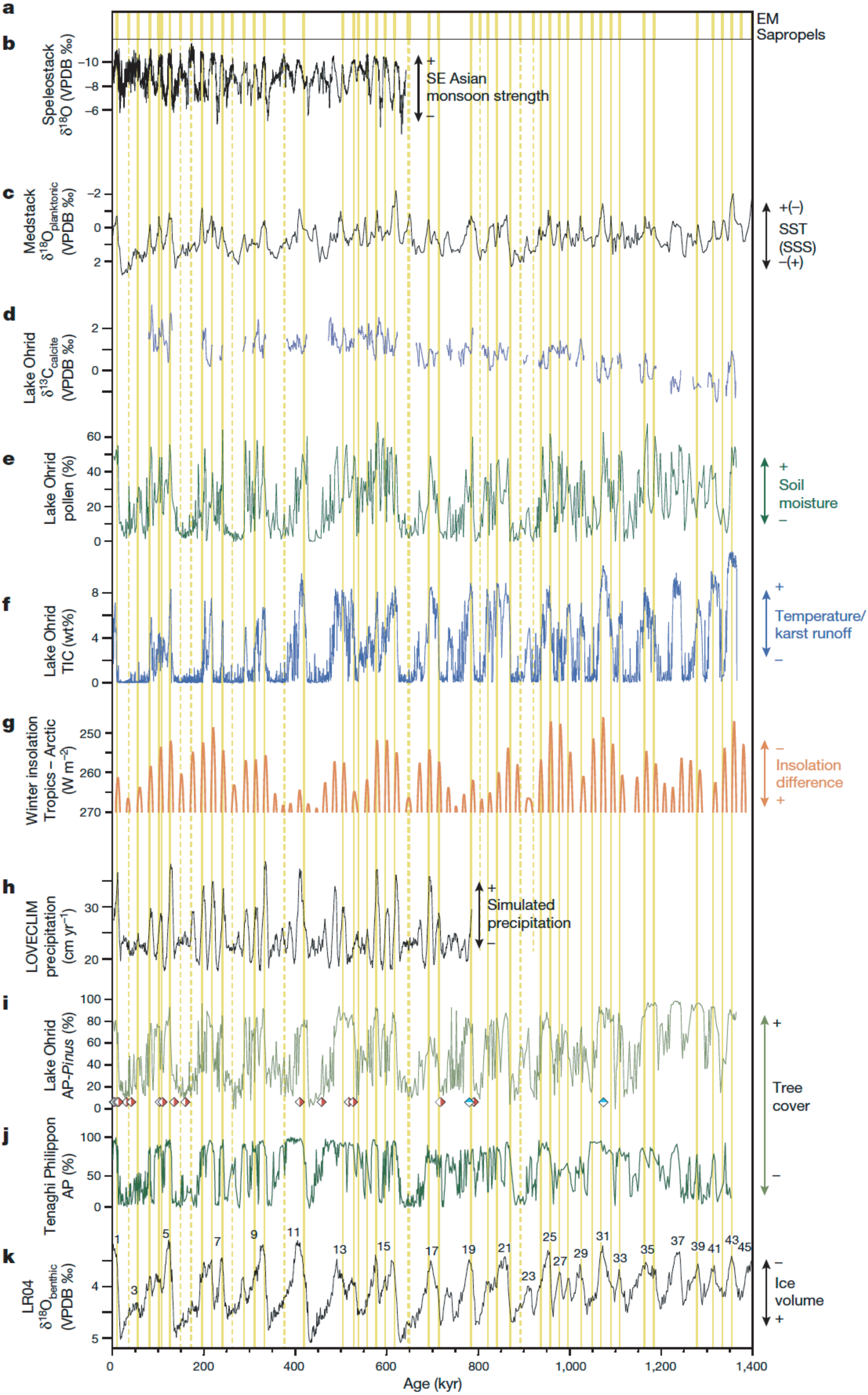

a
EM
Sapropels
b
Speleostack
δ18O (VPDB ‰)
SE Asian
monsoon strength
c
Medstack
δ18O planktonic
(VPDB ‰)
+(–)
SST
(SSS)
–(+)
d
Lake Ohrid
δ13C calcite
(VPDB ‰)
e
Lake Ohrid
pollen (%)
Soil
moisture
f
Lake Ohrid
TIC (wt%)
Temperature/
karst runoff
g
Winter insolation
Tropics – Arctic
(W m−2)
Insolation
difference
h
LOVECLIM
precipitation
(cm yr−1)
Simulated
precipitation
i
Lake Ohrid
AP-Pinus (%)
Tree
cover
j
Tenaghi Philippon
AP (%)
k
LR04
δ18O benthic
(VPDB ‰)
Ice
volume
Age (kyr)

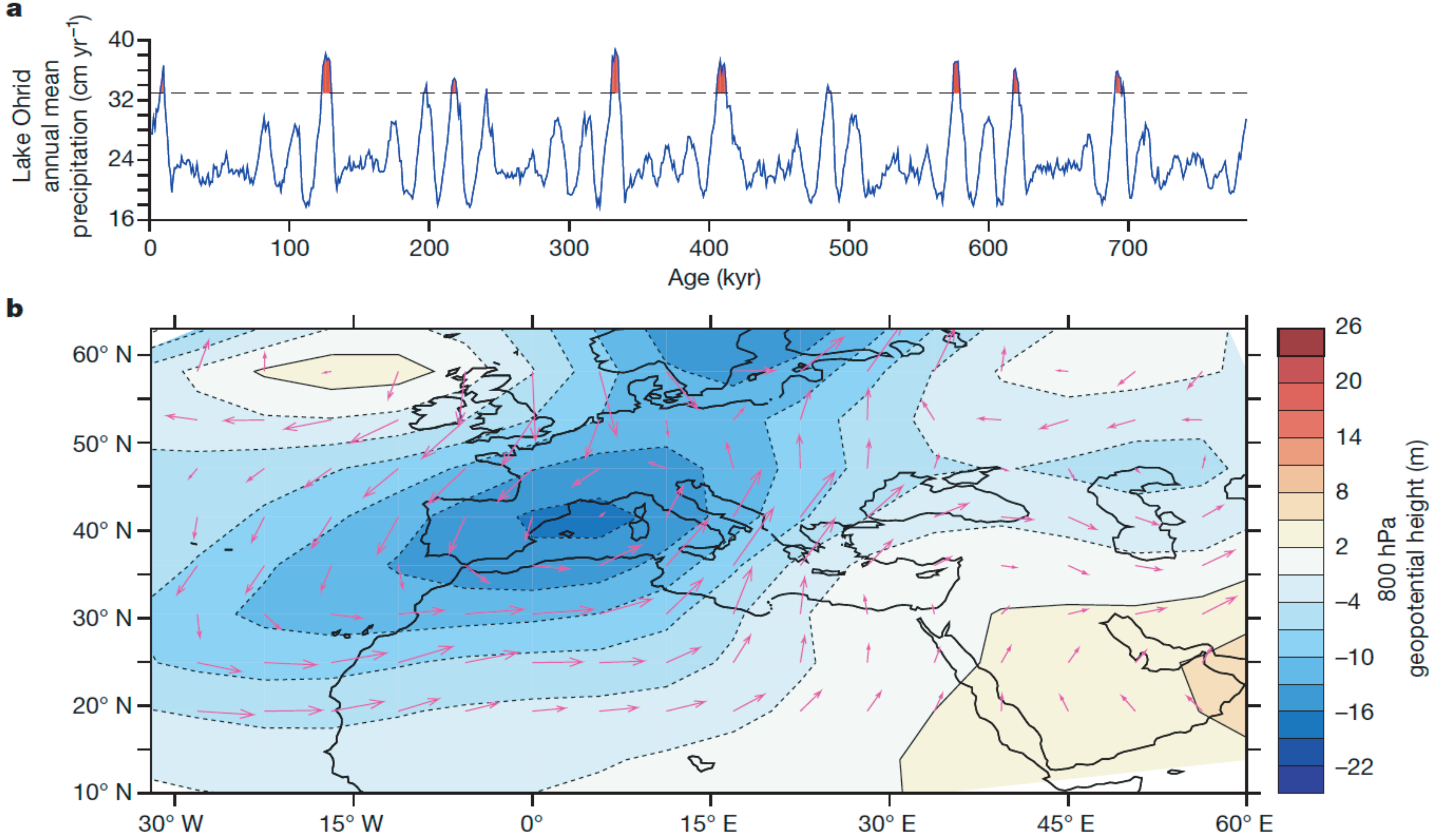
a
Lake Ohrid
annual mean
precipitation (cm yr⁻¹)
40
32
24
16
0
100
200
300
400
500
600
700
Age (kyr)
b
60° N
50° N
40° N
30° N
20° N
10° N
30° W
15° W
0°
15° E
30° E
45° E
60° E
26
20
14
8
2
−4
−10
−16
−22
800 hPa
geopotential height (m)